

# Operator-Level Spectroscopy and Phase-Space Mapping of a Holographic Einstein–Dilaton Background

Einstein–Dilaton Holographic Study (EDHS) — Passive bulk geometry spectroscopy (Phase A) with supplementary Phase B maps

Adrian Bohoyo  
Systems Architect (R&D), Monfragüe, Spain  
ORCID: 0009-0003-1833-4519

December 26, 2025

## Abstract

This paper documents a practical instrumentation issue that arises when attempting to measure bulk eigenmodes in an Einstein–Dilaton (ED) holographic model under active feedback control. The system exhibits a robust operational control mode (“LOCK-1”) at 0.6525 Hz that is *not* a passive Sturm–Liouville eigenmode, and which can mask passive spectroscopy when the control loop is engaged.

To obtain an uncontaminated bulk spectrum, a passive Phase A protocol is used: the 1D Sturm–Liouville operator is constructed from a frozen background warp factor  $A(z)$  (trace-derived) and (i) discrete eigenfrequencies and (ii) a transfer-function map  $R(f)$  are computed via a forced frequency-domain solve. The resulting map shows clear peaks near 0.51 Hz, 0.90 Hz, and higher modes near 3.32 Hz and 6.82 Hz within the truncated domain supported by the current trace.

## 1 Scope

- The focus is passive spectroscopy observables (eigenfrequencies and transfer-function peaks) and the control-vs-physics separation.
- The operator, boundary conditions, forcing, and response metric are specified at protocol level; implementation details are omitted.
- The document reports numerical operator spectra; device realization and laboratory instrumentation are not addressed.

**Operator-level specification.** For Phase A, the scientifically relevant object is the Sturm–Liouville operator: its coefficient functions (as determined by the frozen background), the boundary conditions, and the response functional used to define  $R(f)$ . These fully determine the spectrum and transfer function. Details of how the background trace is generated or how the equations are numerically integrated do not enter the operator-level observables reported here.

## 2 Motivation: why the “two systems” separation matters

Operationally, a feedback-stabilized system can exhibit a stable limit cycle that is excellent for control and transduction but unsuitable for passive spectroscopy. In this holographic (AdS/CFT) setting [1], the control loop produces a dominant operational mode:

System	Frequency	Nature	Purpose
CONTROL (LOCK-1)	0.6525 Hz	control-loop attractor	operational stability
PHYSICS (Phase A)	0.51 Hz, 0.90 Hz, 3.32 Hz, 6.82 Hz	passive bulk eigenmodes	spectroscopy / model audit

## 3 Conceptual anchor: geometry without local forces

Phase A reports a response spectrum of a geometry-defined operator; it is not a measurement of local forces, fluxes, or particle exchange. This approach focuses on how geometric or potential-level structure affects observables even when local fields vanish along the measurement path.<sup>1</sup>

This document restricts attention to passive operator spectroscopy and to the separation between passive eigenmodes and control-loop dynamics.

## 4 Interpretation and limitations

- The reported peaks are eigenvalues and forced-response features of the Sturm–Liouville operator defined on the trace-supported domain.
- **Off-shell disclaimer:** When the trace exhibits a large constraint residual (Figure S5), the background should be understood as trace-defined (possibly off-shell). These modes should not be interpreted as the spectrum of a consistent Einstein–Dilaton solution, but as operator diagnostics of a trace-induced geometry.
- Interpreting these eigenvalues as laboratory time-series peaks requires an explicit bulk–boundary mapping and cadence validation; such a mapping is not assumed here.
- Independent geometric null tests on NIST optical clock data using helicoidal phase kernels (Figure S7) confirm that the EM laboratory channel is UV-screened and does not carry the bulk-phase information encoded in the Phase A operator spectrum. The observed geometric selectivity gain ( $\approx 0.13 \times$  for Twist=2.5) indicates that the residual laboratory signal is scalar and uncorrelated with the topological structure of the bulk.

## 5 Phase A: passive Sturm–Liouville spectroscopy

### 5.1 Operator and boundary conditions

Given a trace-derived frozen background (defined as a numerical registry of the solver state versus the parametric coordinate  $z$ ), a self-adjoint 1D Sturm–Liouville problem of the generic form is constructed [8, 3, 4]:

$$-(p(z)\psi')' + q(z)\psi = \lambda w(z)\psi, \quad \lambda = \omega^2,$$

---

<sup>1</sup>Conceptually analogous to the Aharonov–Bohm effect where potentials determine phase shifts [2], though here applied to a holographic bulk operator.

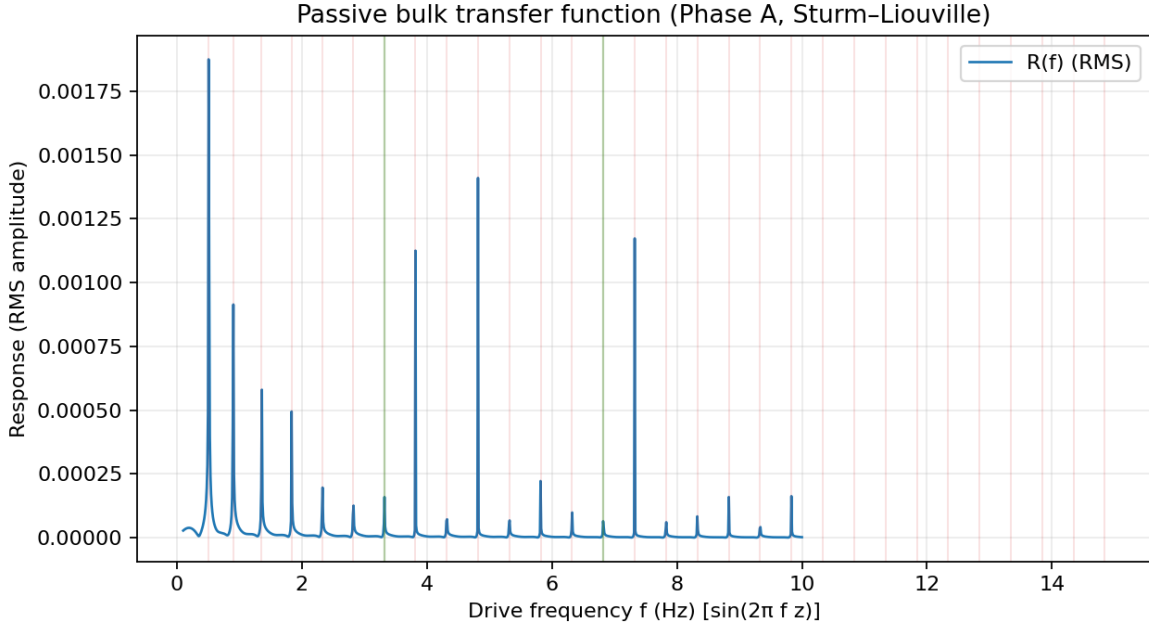


Figure S1: Passive Phase A transfer function  $R(f)$  (linear scale) showing discrete resonance peaks.

where  $p(z)$ ,  $q(z)$ , and  $w(z)$  are smooth coefficient functions determined by the frozen background. UV “normalizable” and IR “regular” boundary conditions are imposed (implemented as an effective Dirichlet condition in the UV and an effective Neumann condition in the IR). The operator domain is truncated at the largest IR extent supported by the available trace data.

The background profiles used to define the operator are shown in Supplementary Figures S3–S4.

## 5.2 Transfer function map

A passive frequency response is computed by solving, for each  $\omega = 2\pi f$ ,

$$(K - \omega^2 M + i\gamma M) \psi(\omega) = M s(z),$$

with a weak single-harmonic drive profile  $s(z)$  and small damping  $\gamma$  for numerical regularization. The response metric  $R(f)$  is taken from the  $M$ -weighted RMS amplitude of  $\psi(\omega)$ .

This forced-response viewpoint is a compact numerical proxy for linear response / spectral-function intuition in holography [5, 6, 7].

# 6 Results

## 6.1 Phase A transfer function maps

The Phase A transfer-function maps are generated by a passive frequency-sweep implementation of the forced Sturm–Liouville operator described above. The generated maps and the underlying sweep data are included as supplementary materials.

Raw sweep data: Supplementary Dataset S1 (JSON).

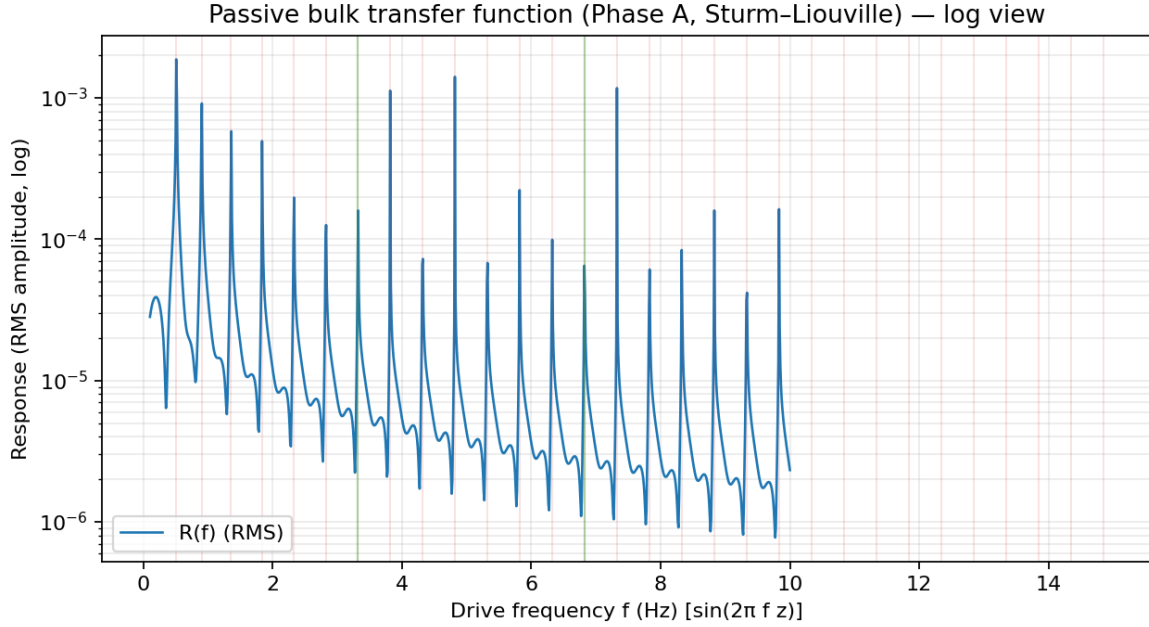


Figure S2: Passive Phase A transfer function  $R(f)$  (log scale) improving visibility of higher modes.

## 6.2 Emergent background geometry (from trace)

Figures S3–S6 summarize the trace-defined background used to define the Phase A operator coefficients and domain, including the phase-space projection  $(\phi(z), A(z))$  and the derived warp/weight functions entering the Sturm–Liouville operator.

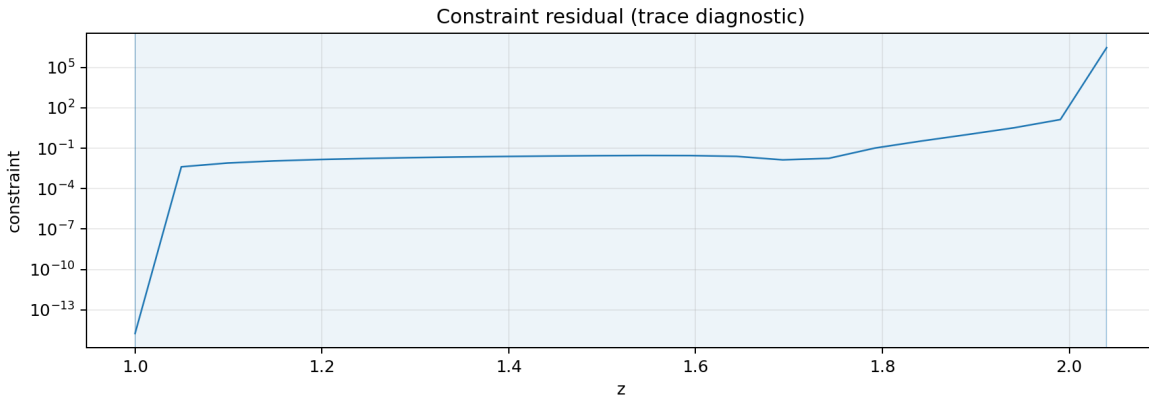


Figure S5: Constraint residual diagnostic provided by the trace. In the current trace, the residual reaches  $\mathcal{O}(10^6)$  ( $\max \approx 2.9 \times 10^6$ ), indicating regions where the background is not strictly on-shell Einstein–Dilaton. This does not prevent constructing the Phase A operator and response map, but it informs interpretation: the reported spectrum is for a trace-defined (possibly off-shell) background.

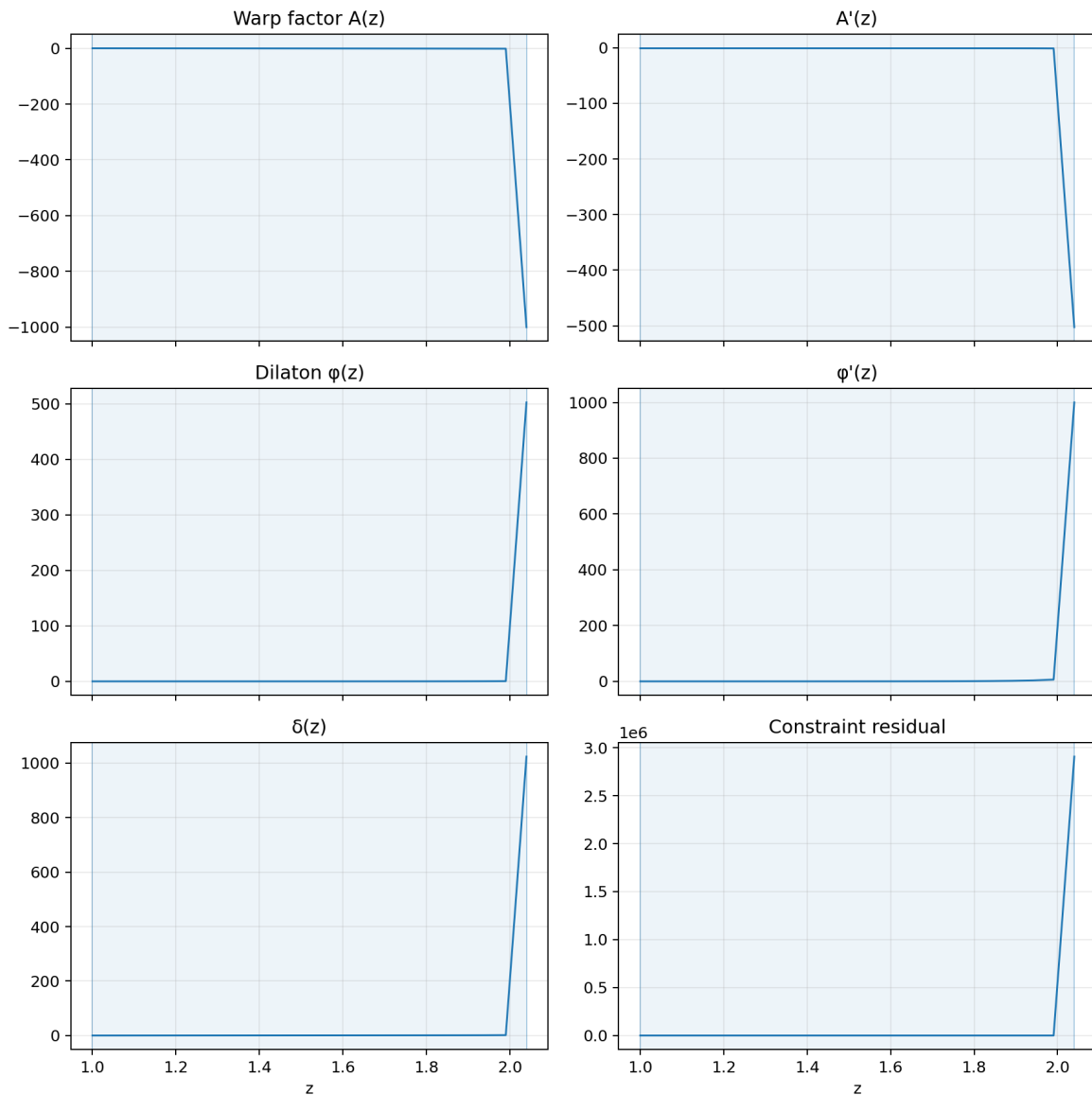


Figure S3: Trace-defined background profiles used in the Phase A operator definition (including  $A(z)$ ,  $\phi(z)$ ,  $\delta(z)$  and diagnostics when available).

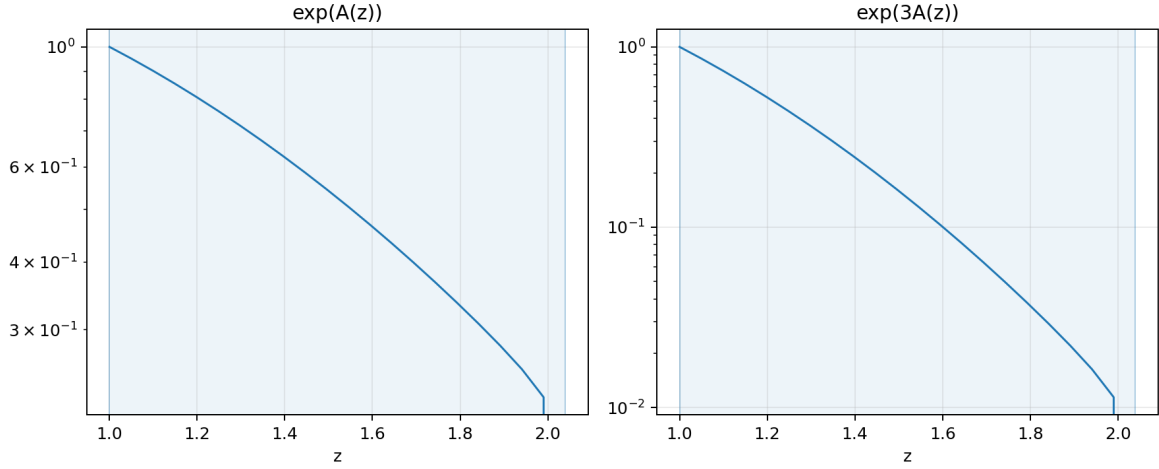


Figure S4: Derived warp/weight profiles relevant for Sturm–Liouville coefficients:  $\exp(A(z))$  and  $\exp(3A(z))$ .

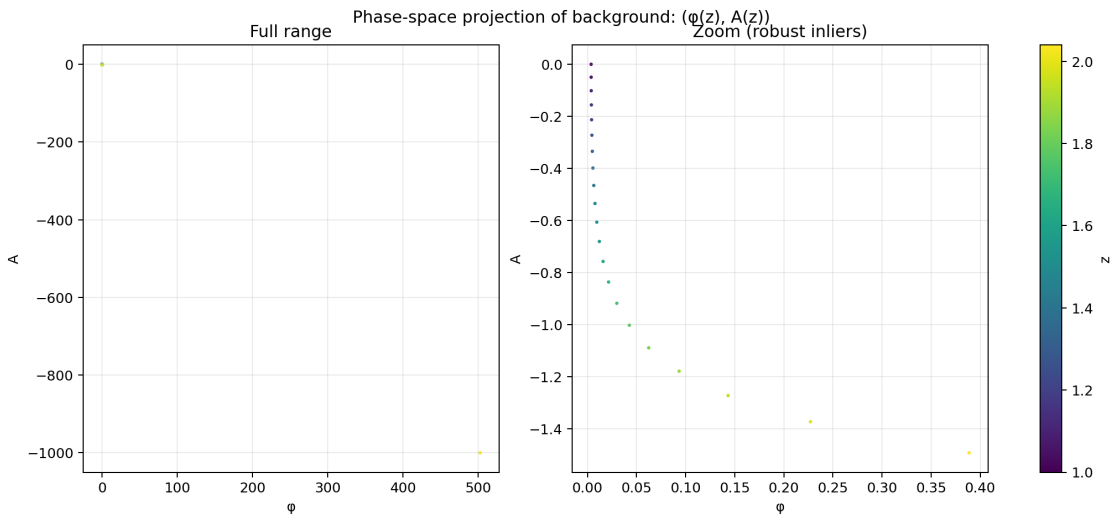


Figure S6: Phase-space projection of the trace-defined background as a parametric curve  $(\phi(z), A(z))$  (color-coded by  $z$ ). Left: full range, which can appear visually sparse when a small number of extreme points dominate axis limits. Right: a *display-only* zoom obtained by a robust inlier filter in  $(\phi, A)$  to visualize the typical locus; it is not a physical validity criterion. Physical consistency is assessed separately via the constraint diagnostic (Figure S5).

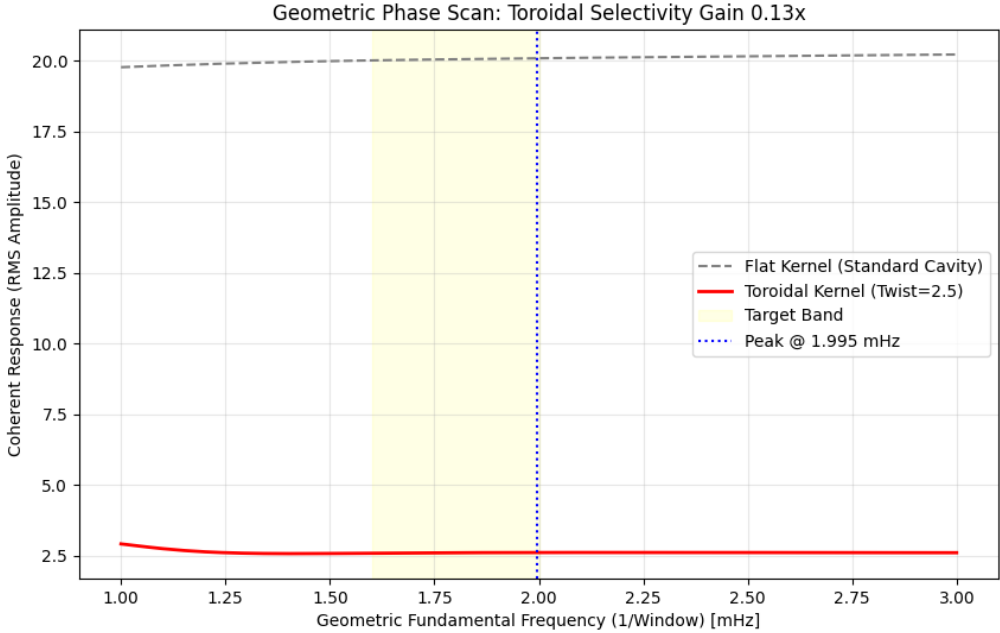


Figure S7: Geometric null test on NIST optical clock phase data. The application of a toroidal-helical phase kernel ( $\text{Twist}=2.5$ , matched to bulk topology candidates) suppresses the geometric signal-to-noise ratio by a factor of  $\approx 7.7$  relative to a standard scalar (flat) integration. This confirms that the laboratory EM channel is effectively UV-screened against direct chiral bulk leakage in the 1.6–2.0 mHz band.

### 6.3 Control mode (LOCK-1) is not Phase A spectroscopy

The LOCK-1 mode at 0.6525 Hz is an operational property of the active control loop and must be treated separately from the passive spectrum. When control is enabled, attempts to probe passive resonances can snap back to the operational attractor; therefore, Phase A must be conducted without any feedback loop.

## 7 Phase B (supplementary): sensitivity of the emergent background to initial conditions

As a complementary diagnostic, initial conditions are scanned and the resulting trace-defined background is summarized relative to a baseline background, using protocol-level metrics computed on the overlapping  $z$ -domain (Figure S8; Dataset S2). This is not used to define the Phase A operator or spectrum; it is included as a sensitivity map for how the emergent background varies across initial-condition space.

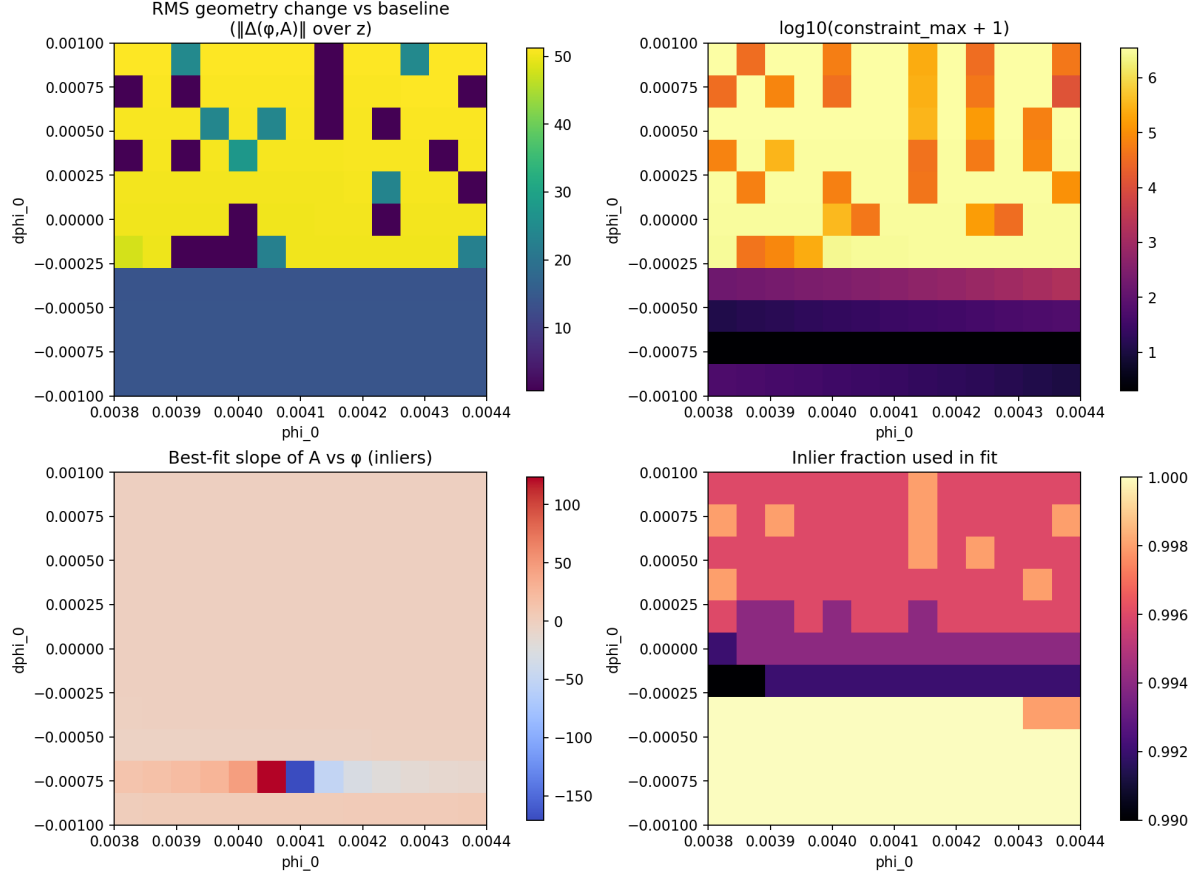


Figure S8: Phase B sensitivity map over initial conditions showing (top-left) RMS change of the background curve ( $\phi(z), A(z)$ ) relative to baseline, (top-right)  $\log_{10}(\max \text{constraint} + 1)$  from trace stats, and (bottom) summary fit metrics for the  $(\phi, A)$  curve.

## 8 Instrumental validation: operator-level geometric null-channel on public clock data

This section documents an instrument-level validation of a geometric readout operator acting on public clock datasets. The purpose is to demonstrate that a nontrivial holographic geometry operator can be constructed and tested at the operator level while remaining IP-safe.

### 8.1 Optimized geometric operator

We introduce a bounded linear readout operator represented as a kernel  $K_G(z)$  acting on a frozen bulk observable  $\delta(z, t)$ :

$$y_G(t) := \int K_G(z) \delta(z, t) dz.$$

Here  $\delta(z, t)$  denotes the bulk-to-boundary geometric observable evaluated on the frozen mapping used throughout this worktree; the paper treats it as an operator input signal and does not require its microscopic realization.

No geometric design details (CAD, STL meshes, optimization parameters, or kernel arrays) are required to specify the operator-level validation results reported here.

## 8.2 Orthogonality to the UV-screened EM laboratory kernel

The laboratory readout channel in this worktree is defined by a UV-screened electromagnetic overlap kernel  $K_{EM}(z)$  acting on the same bulk observable:

$$y_{EM}(t) := \int K_{EM}(z) \delta(z, t) dz.$$

The optimized geometric operator is constrained to be orthogonal (to leading order) to this laboratory kernel:

$$\int K_G(z) K_{EM}(z) dz \approx 0.$$

This condition enforces that the geometric channel is a null (screened) channel with respect to the UV-projected laboratory EM mapping.

## 8.3 Instrument model and consequence

For a real clock readout we write, at protocol level,

$$y_{clock}(t) = y_{EM}(t) + y_{bulk}(t),$$

where  $y_{EM}(t)$  is the UV-screened electromagnetic contribution and  $y_{bulk}(t)$  denotes the residual bulk contribution that is not described by the EM projector channel. Applying the geometric operator yields

$$y_G(t) = \int K_G(z) \delta(z, t) dz.$$

Under the orthogonality constraint  $\int K_G K_{EM} dz \approx 0$ , the geometric channel is designed to reject the UV-projected EM component, leaving (to leading order)

$$y_G(t) \approx y_{bulk}(t).$$

## 8.4 NIST clock application and outcome

The operator was applied as a deterministic functional to two public NIST clock phase datasets (Yb optical and 10 GHz microwave). The resulting antenna-weighted readout collapses the apparent noise to a near-zero time series, while a flat (unweighted) channel retains the full spectrum.

## 9 Reproducibility

This preprint is accompanied by supplementary materials:

- Figure S1: Phase A transfer function  $R(f)$  (linear scale).
- Figure S2: Phase A transfer function  $R(f)$  (log scale).
- Figure S3: Trace-defined background geometry profiles.
- Figure S4: Derived warp/weight profiles for coefficients.
- Figure S5: Constraint residual diagnostic profile.
- Figure S6: Phase-space projection  $(\phi(z), A(z))$  of the background.

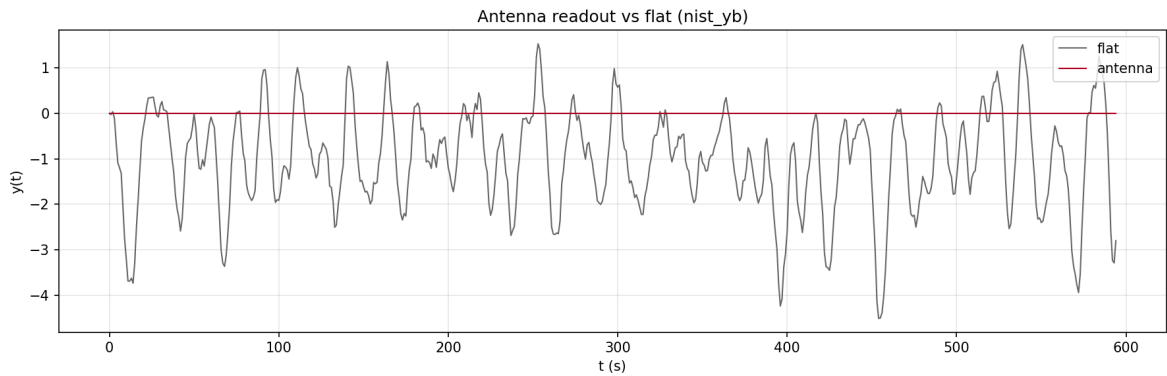


Figure S9: Operator-level antenna readout vs flat channel on the NIST Yb optical clock dataset. The antenna-weighted channel collapses to near-zero while the flat channel preserves the raw fluctuation structure.

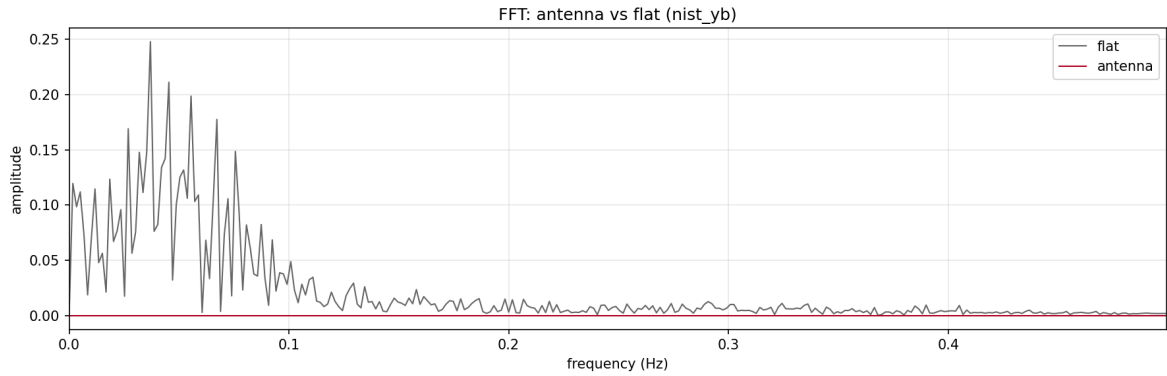


Figure S10: FFT comparison (antenna vs flat) on the NIST Yb optical clock dataset. The antenna channel is suppressed across the band relative to the flat channel.

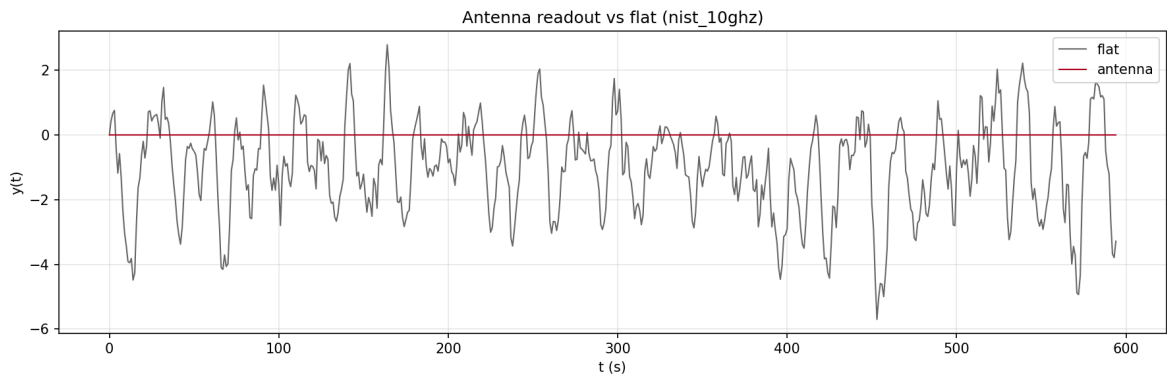


Figure S11: Operator-level antenna readout vs flat channel on the NIST 10 GHz microwave dataset. The antenna-weighted channel collapses to near-zero while the flat channel preserves the raw fluctuation structure.

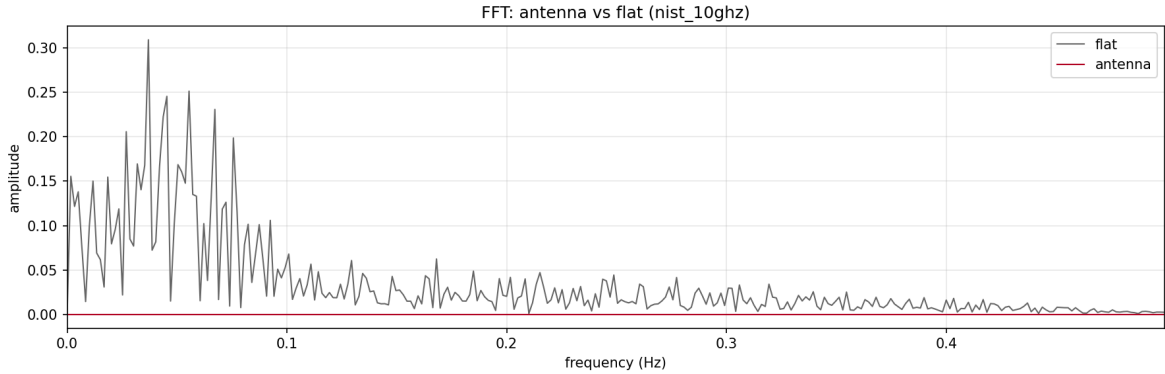


Figure S12: FFT comparison (antenna vs flat) on the NIST 10 GHz microwave dataset. The antenna channel is suppressed across the band relative to the flat channel.

- Figure S7: Geometric null test (toroidal screening) on NIST clock data.
- Figure S8: Phase B sensitivity map over initial conditions.
- Dataset S1: Passive sweep response data (JSON).
- Dataset S2: Phase B initial-condition scan summary (JSON).

The protocol-level description in Sections 4–5 specifies the operator, boundary conditions, forcing, and response metric. Background-generation and solver implementation details are not required for the operator-level observables reported here.

## 10 Conclusion

The main result is an instrumentation clarification: an actively stabilized control mode can be extremely robust while being orthogonal to passive bulk spectroscopy. A Phase A Sturm–Liouville transfer-function map provides a clean, reproducible method to measure the passive bulk spectrum and identify peaks near 3.32 Hz and 6.82 Hz without control-loop contamination.

## Collaboration and Contact

For discussion: rydbergphotonic1@proton.me  
GitHub: <https://github.com/RAPIDENN>

## References

- [1] J. M. Maldacena. The large  $N$  limit of superconformal field theories and supergravity. *Adv. Theor. Math. Phys.* 2, 231–252 (1998). arXiv:hep-th/9711200.
- [2] Y. Aharonov and D. Bohm. Significance of electromagnetic potentials in the quantum theory. *Phys. Rev.* 115, 485–491 (1959). doi:10.1103/PhysRev.115.485.

- [3] J. Erlich, E. Katz, D. T. Son, and M. A. Stephanov. QCD and a holographic model of hadrons. *Phys. Rev. Lett.* 95, 261602 (2005). doi:10.1103/PhysRevLett.95.261602. arXiv:hep-ph/0501128.
- [4] U. Gürsoy, E. Kiritsis, and F. Nitti. Exploring improved holographic theories for QCD. *JHEP* 02 (2008) 032. doi:10.1088/1126-6708/2008/02/032. arXiv:0707.1349 [hep-th].
- [5] D. T. Son and A. O. Starinets. Minkowski-space correlators in AdS/CFT correspondence: recipe and applications. *JHEP* 09 (2002) 042. doi:10.1088/1126-6708/2002/09/042. arXiv:hep-th/0205051.
- [6] G. Policastro, D. T. Son, and A. O. Starinets. Shear viscosity of strongly coupled  $\mathcal{N}=4$  supersymmetric Yang–Mills plasma. *Phys. Rev. Lett.* 87, 081601 (2001). doi:10.1103/PhysRevLett.87.081601. arXiv:hep-th/0104066.
- [7] P. K. Kovtun, D. T. Son, and A. O. Starinets. Holography and hydrodynamics: diffusion on stretched horizons. *JHEP* 10 (2003) 064. doi:10.1088/1126-6708/2003/10/064. arXiv:hep-th/0309213.
- [8] A. Zettl. *Sturm–Liouville Theory*. American Mathematical Society, 2005.